Supplementary data for the article:

"Quantitative analysis of the evolution of ASR products and crack networks in the context of the concrete mesostructure"

Mahdieh Shakoorioskooie[a,b,c], Michele Griffa[a], Andreas Leemann[a], Robert Zboray[b], Pietro Lura[a,c]

[a] *Concrete and Asphalt Laboratory, Empa, Swiss Federal Laboratories for Materials Science and Technology, CH-8600 Dübendorf, Switzerland*

[b] *Center for X-ray Analytics, Empa, Swiss Federal Laboratories for Materials Science and Technology, CH-8600 Dübendorf, Switzerland*

[c] *Institute for Building Materials (IfB), ETH Zürich, CH-8093 Zürich, Switzerland*

S1. Aggregates-to-cement paste contrast optimization by $BaSO_4$ concentration selection and assessment of its effects on the ASR (cracking)

S1.1. Mix composition of the specimens cast with P aggregates and with $BaSO_4$

Table S1. Mix composition of the $BaSO_4$-containing specimens cast with the P aggregates, in units of kg·m^{-3} (mass per m^3 of cast material).

Specimen label	Cement CEM I 42.5N	Aggregates			Deionized water	NaOH	$BaSO_4$
		0 – 4 mm	4 – 8 mm	8 – 11.25 mm			
$\boldsymbol{P-0.25\ vol.\%\ BaSO_4}$	450	656	410	574	225	4.9	7.20
$\boldsymbol{P-0.75\ vol.\%\ BaSO_4}$	450	650	406	569	225	4.9	21.27
$\boldsymbol{P-1.5\ vol.\%\ BaSO_4}$	450	641	401	561	225	4.9	42.38
$\boldsymbol{P-2.5\ vol.\%\ BaSO_4}$	450	630	394	552	225	4.9	70.05
$\boldsymbol{P-3\ vol.\%\ BaSO_4}$	450	625	390	547	225	4.9	83.8

S1.2. SEM/EDX analysis of raw materials and of the ASR products

SEM-BSE was used both to assess the size range of the $BaSO_4$ grains and to characterize qualitatively their spatial distribution in the concrete specimens cast with it. The respective images were acquired with a FEI Quanta 650 ESEM, by Thermo Fisher Scientific, equipped with an EDX detector (Thermo Noran Ultra Dry 60 mm^2), available at Empa's Electron Microscopy Center (https://www.empa.ch/web/s299/info). The electron beam acceleration voltage was set to 20 kV.

Figure S1 shows SEM-BSE micrographs of the $BaSO_4$ powder's grains compared against the cement's ones, insets (a) and (b), respectively. The $BaSO_4$ grain size was at the scale of about 1 µm. Insets (c) and (d) in the same figure show regions of interest (ROIs) in the cement paste of one U-3 vol.% $BaSO_4$ specimen at 40 days from casting (i.e., 39 days of ASR acceleration). The $BaSO_4$ grains had larger BSE pixel value than any other material phase because of their larger electron density, compared with the un-hydrated cement grains, which are by themselves denser than the cement hydrates. From insets (c) and (d), it is possible to assess that the $BaSO_4$ grains (the brightest, small spots) were homogeneously dispersed throughout the cement paste and seemed not to have interacted at all with the hydrating cement, as expectable based upon what already reported in the literature [1].

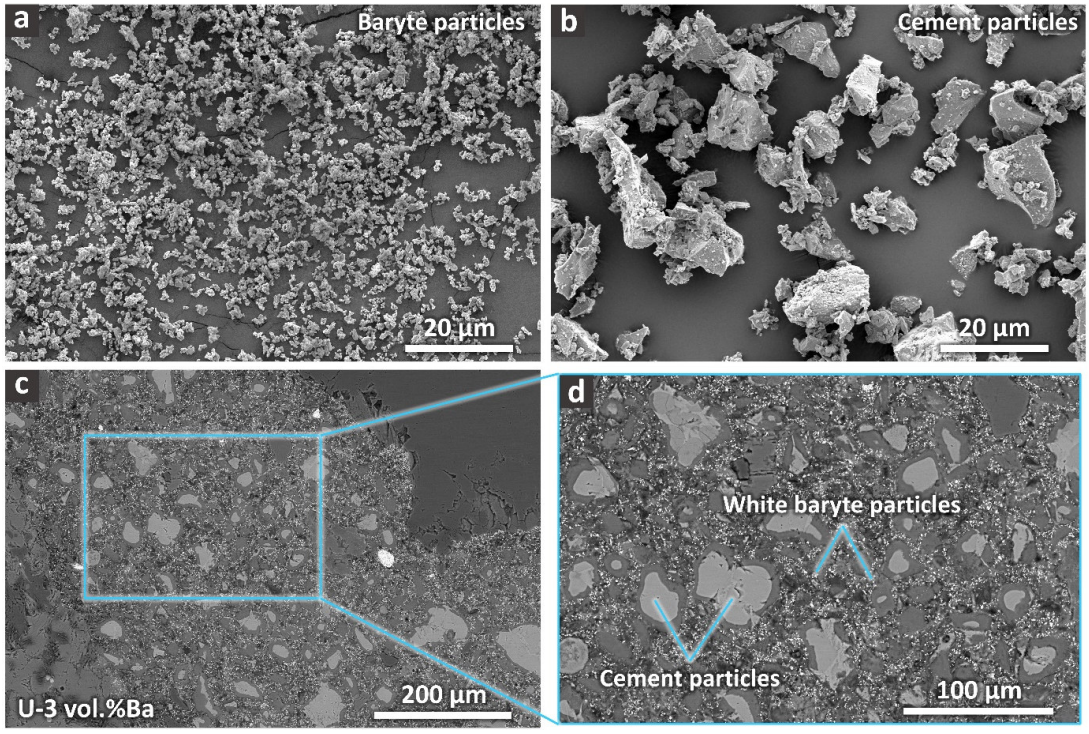

Figure S1. An example of SEM-BSE micrographs of (a) the used $BaSO_4$ powder, (b) the used cement powder, for comparison, (c) the cross-section of a specimen cast with 3 vol.-% of $BaSO_4$, prepared at

40 days from casting, and (d) a region of interest of inset (c) to highlight the spatial distribution of the $BaSO_4$ grains across the cement paste.

SEM-BSE was also exploited to analyse the morphology of the ASR products formed in specimens cast with and without $BaSO_4$. Figure S2 shows in some of such micrographs ASR products inside cracks in specimens at 120 days, cast both without and with $BaSO_4$ at a concentration of 2.5 vol.-%. All micrographs were acquired for aggregate interior regions, where the ASR products are expected to be rather crystalline, with a plate-like morphology. Regardless of the $BaSO_4$ absence or presence, the ASR products exhibited analogous morphology and BSE contrast inside the aggregates. This result suggests that no significant perturbation of ASR took place because of the presence of $BaSO_4$ in the cement paste, in agreement with the available knowledge from the literature about its very low solubility in aqueous environments [2].

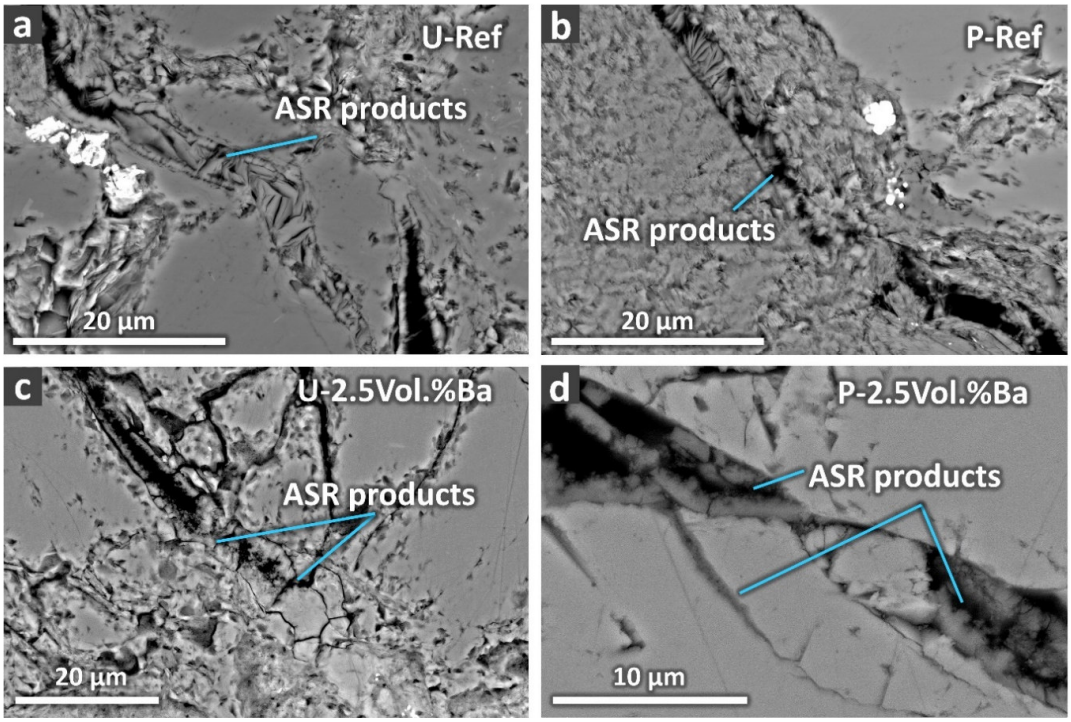

Figure S2. SEM-BSE micrographs providing examples of the distribution of ASR products inside cracks of specimens containing both aggregate types and either without or with $BaSO_4$. For every specimen type, the micrographs were acquired at 120 days. Micrographs for (a) U-Ref, (b) P-Ref, (c) U-2.5 vol.-% $BaSO_4$, (d) P-2.5 vol.-% $BaSO_4$, respectively.

The EDX point analysis of ASR products in different regions of distinct specimens, without and with BaSO4, confirmed their similarity in terms of chemical composition. Figure S3 shows ternary diagrams, obtained by such EDX analysis. As it is observed in such ternary diagrams, the ASR products compositions was almost identical regardless of aggregate type and of the presence or not of $BaSO_4$. No sign of Ba^{+} or SO^{4-} incorporation into the ASR products was detected, providing additional evidence of the $BaSO_4$ chemical stability in the concrete aqueous environment.

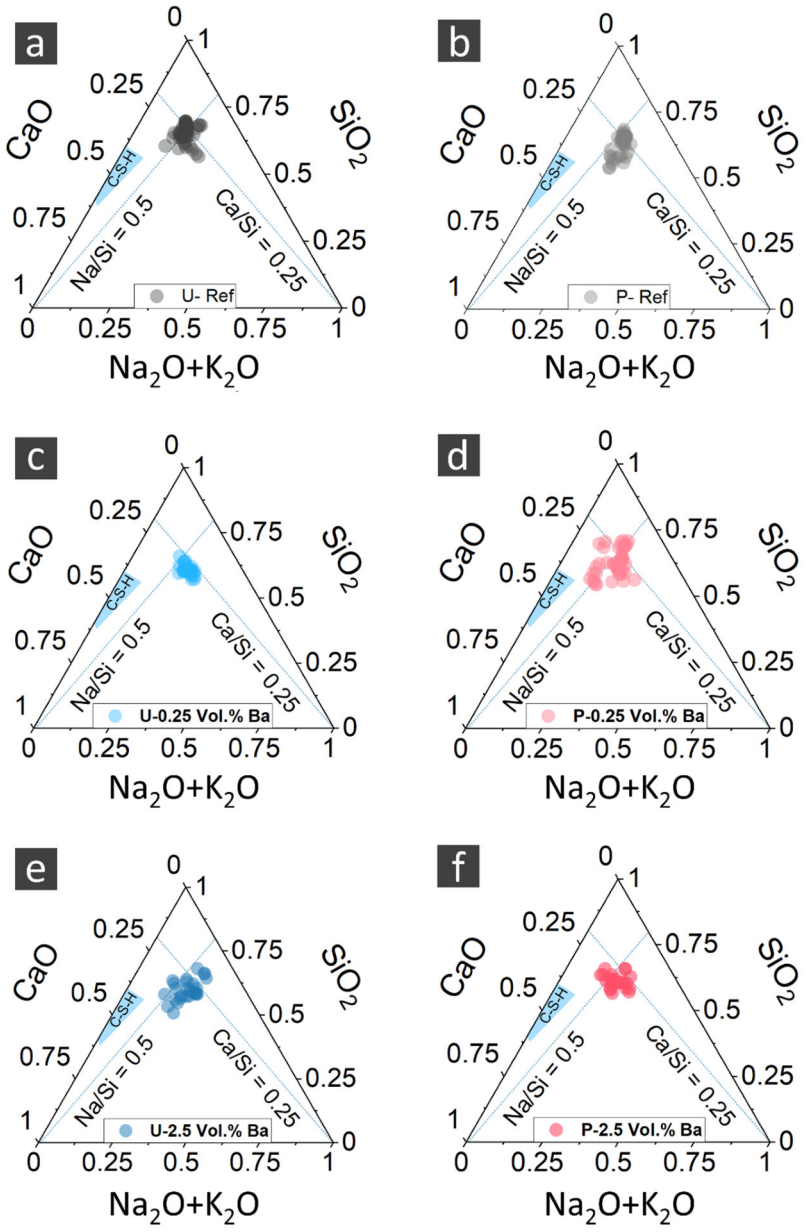

Figure S3. EDX analysis results showing the equivalent sodium oxide ternary diagrams for ASR products located at more than 30 points and both of crystalline type (i.e., inside the aggregates) and

of amorphous type (at the aggregate boundary regions and in the cement paste). The investigated specimens were cast with both aggregate types and without or with two $BaSO_4$ concentrations. (a) U-Ref, (b) P-Ref, (c) U-0.25 vol.-% $BaSO_4$, (d) P-0.25 vol.-% $BaSO_4$, (e) U-2.5 vol.-% $BaSO_4$, (f) P-2.5 vol.-% $BaSO_4$ specimens, respectively.

S1.3. Time-lapse XT

Reference specimens

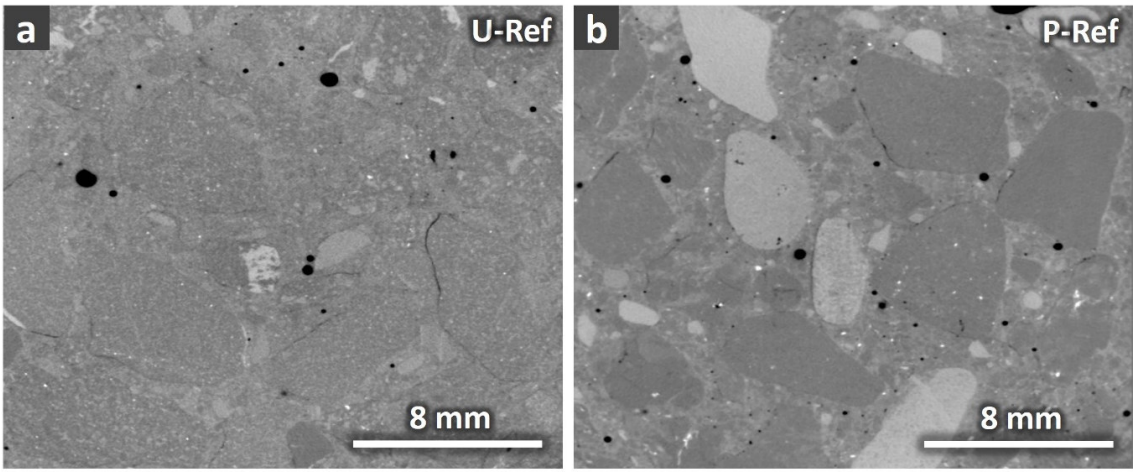

Figure S4. A ROI example on a tomographic slice from (a) one U-Ref specimen and (b) a P-Ref one. The tomograms of both specimens were acquired at the reference time point t_0= 1 day since the ASR acceleration start. These examples clearly show the almost complete absence (in the U-Ref specimen case) or very low image contrast between aggregates and cement paste, in the absence of $BaSO_4$ added to the mix design.While in the U-Ref case only the boundaries of some aggregates allow to identify them. In the P-Ref one, some aggregate bear sufficiently larger X-ray attenuation than the surrounding cement paste, others not. On average, aggregates in the latter specimen are more easily recognizable than in the former, mainly because of higher mineralogical heterogeneity.

S1.4. Influence of the $BaSO_4$ concentration on the X-ray attenuation contrast

By comparing Figure S4 (a) with Figures S5 (a) to (e), it is possible to observe that the addition of $BaSO_4$ to the mix did not provide any enhancement of the X-ray attenuation contrast in the tomograms of the U specimens when its concentration was smaller than or equal to 0.25 vol.-%. The same result was obtained for the tomograms of the P specimens, as evident when comparing Figure S4 (b) with Figures S6 (a) to (e).

The segmented aggregates volume fraction approached the mix design's nominal value at about 2.5 vol.-% also for the P specimens' tomograms, as occurred for the U specimens'.

Contrary to what occurred with the U specimen's tomograms, the segmented aggregates volume fraction was already rather high (about 52 vol.-%) in correspondence of the minimum concentration of 0.25 vol.-% and increased much more slowly with increasing concentration, as shown in Figure S7 (b).

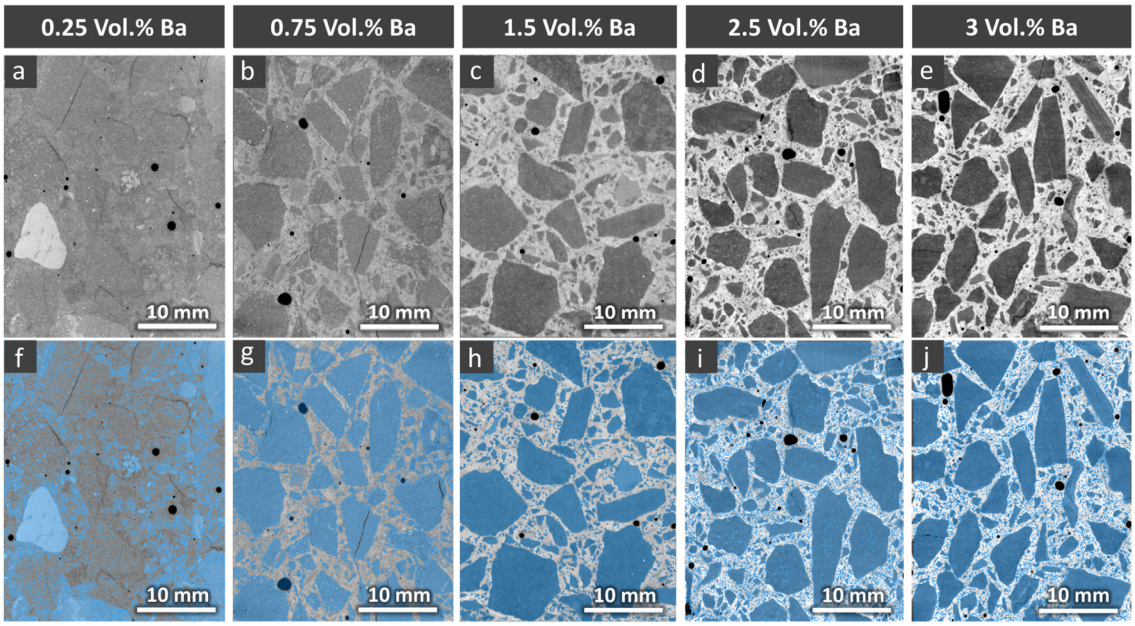

Figure S5. (a) to (e): examples of ROIs on tomographic slices at 150 days of ASR acceleration, from specimens cast with the U aggregates and with various $BaSO_4$ concentrations. These ROIs are containing also the ones shown in Figure 1 in the article. (f) to (j): the same slices as in (a) to (e) but, additionally, with the corresponding slices from the binary tomograms of the segmented aggregates, rendered as semi-transparent, in blue and overlaid on top of the original tomographic slices.

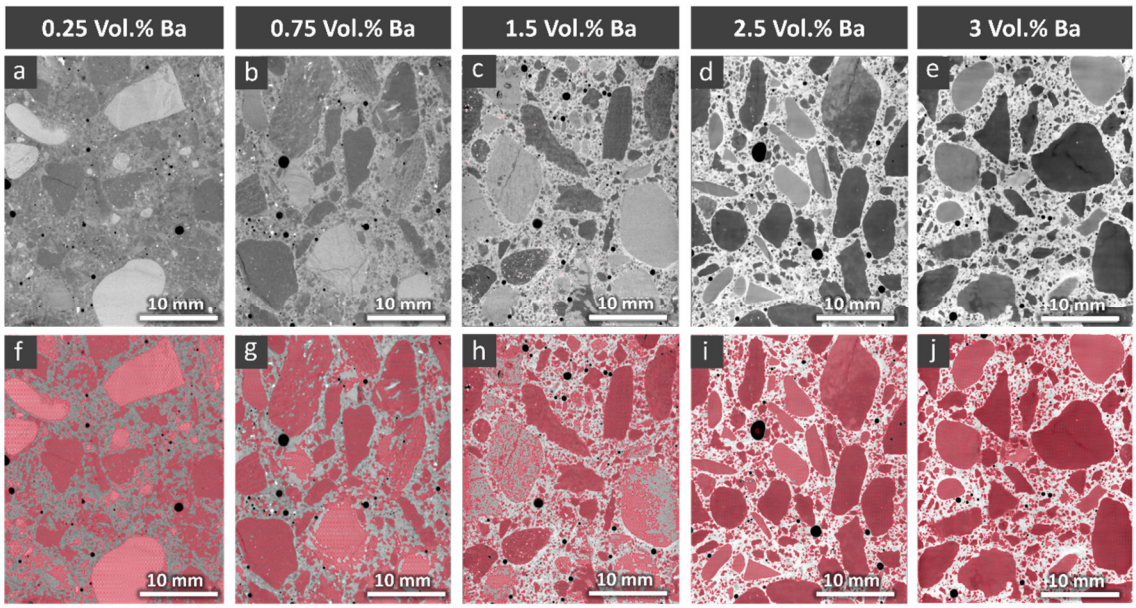

Figure S6. Similar figure as Figure S5 but for the specimens cast with the P aggregates.

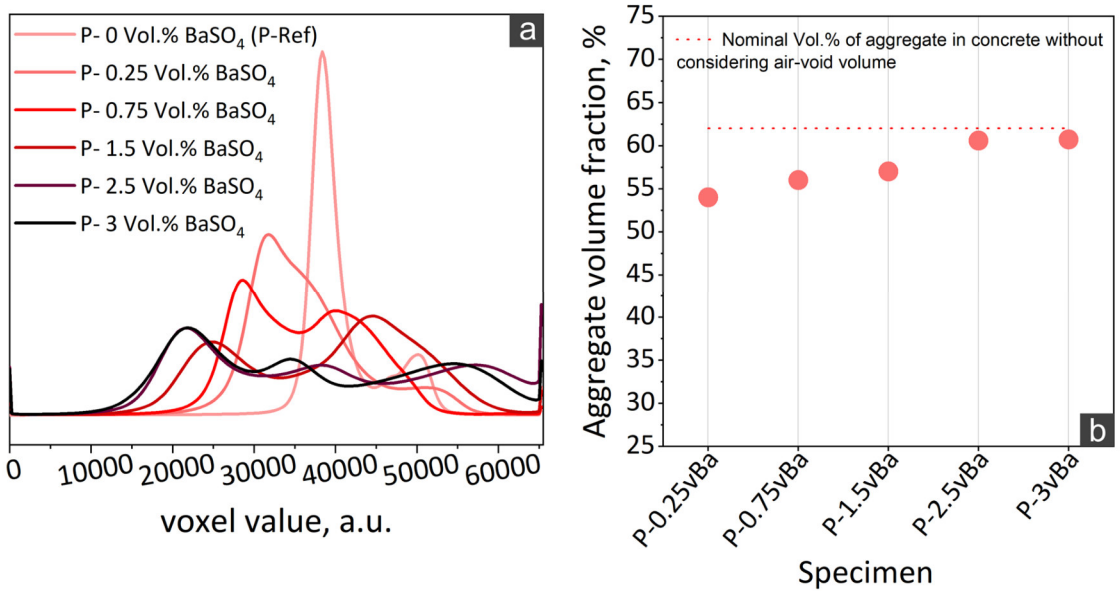

Figure S7. *(a) Full tomogram voxel value histograms for the specimens cast with various $BaSO_4$ concentrations (0.25, 0.75, 1.5, 2.5 and 3 vol.%) and with P aggregates. Each histogram refers to the tomogram of a single specimen at 150 days of ASR acceleration. (b) Volume fraction of segmented aggregates, defined as the volume of segmented aggregates divided by the full tomogram's volume of the tomogram. The dotted horizontal line about 62% indicates the aggregate volume fraction of the full specimen, calculated based upon the mix design by ignoring air voids.*

S1.5. ASR-induced global deformations and mechanical properties changes: $BaSO_4$ concentration influences

Independently of the aggregate type, the addition of $BaSO_4$ to the mix design, within the tested concentration ranges, did not have any significant influence on the whole specimen scale expansion, as already shown in Figure 3 within the article (for the U specimens) and as shown in Figure S8 (for the P specimens). As already noted in correspondence of Figure 1 within the article, at any time point, the relative length change, $\frac{\Delta L_Z}{L_Z}$, of the P specimens also varied randomly with varying $BaSO_4$ concentration but the fluctuations had amplitude of the same order of magnitude of the error bar size due to the specimen realization, i.e., due to the intrinsic material structure heterogeneity. Slightly higher amplitude fluctuations were observed, at any time point, for the relative mass change of the same specimens for which the $\frac{\Delta L_Z}{L_Z}$ time series were measured, as observable in Figure S9 for both aggregate types. Still, they were still random fluctuations with varying $BaSO_4$ concentration, again pointing to the absence of its effects on the ASR development.

Concerning differences between specimens cast with the two distinct aggregate types, those produced with U aggregates expanded faster than those with P aggregates, as already reported in [3]. The former specimens reached a maximum expansion level almost double the one of the latter, at 250 days. The higher expansion rates for the specimens cast with U aggregates than for those cast with P aggregates are attributed to their differences in the mineralogical texture. As sedimentary rocks, the U aggregates contains a higher volume fraction of grain boundaries, which can facilitate silica dissolution, thus increasing the ASR rates and the corresponding expansion. Such explanation is also supported by the higher increase in specimen mass for the U specimens compared with the P ones, as shown in Figure S9, which is to be expected since grain boundaries favour liquid transport through the specimens.

Additional evidence of the absence of spurious effects of the $BaSO_4$ addition on the ASR expansion is provided by the time series of the relative size change, along the X and Y directions, of the tomographed regions of the distinct specimens, as estimated from the global affine registration results ($\frac{\Delta L_{AFF,k}}{L_{AFF,k}}, k = X\ or\ Y$). Figure S10 (a) and (c) show such time series for the U-Ref and the U-2.5 vol.-% $BaSO_4$ specimens, respectively. Figure S10 (b) and (d) show the time series for the corresponding P specimens. For any aggregate type, the tomographed regions expanded laterally rather similarly, independently of the absence or presence of $BaSO_4$ in the mix design. We assume that such result was also representative for the whole specimen volume. Indeed, the $\frac{\Delta L_Z}{L_Z}$ time series and the $\frac{\Delta L_{AFF,z}}{L_{AFF,z}}$ ones strongly overlapped on top of each

other, as also shown in Figure S10, signalling that, at least along the Z-axis, the expansion of the tomographed region occurred rather similarly as for the whole specimen. We consider as very likely that such a result held also along the two lateral directions, X and Y.

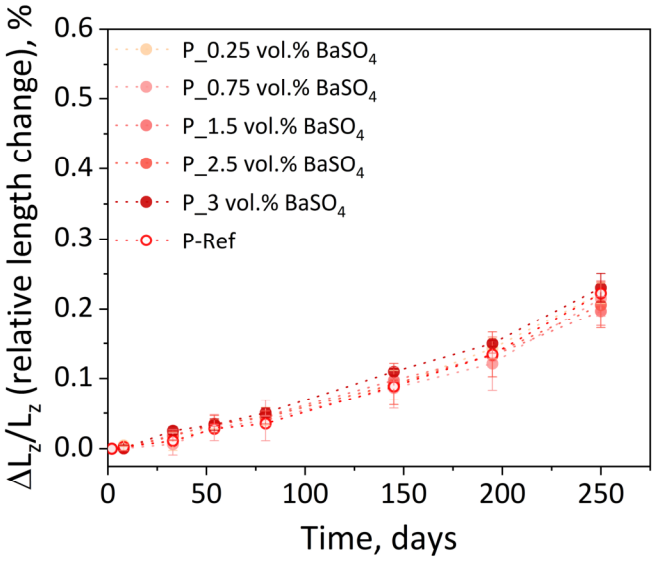

Figure S8. Evolution of the relative specimen length change, $\frac{\Delta L_z}{L_z}$, for the P specimens with (filled markers) or without (hollow marker) $BaSO_4$. The markers indicate mean values while the error bars' size is the standard deviation of an ensemble of six distinct specimens, for each specimen set.

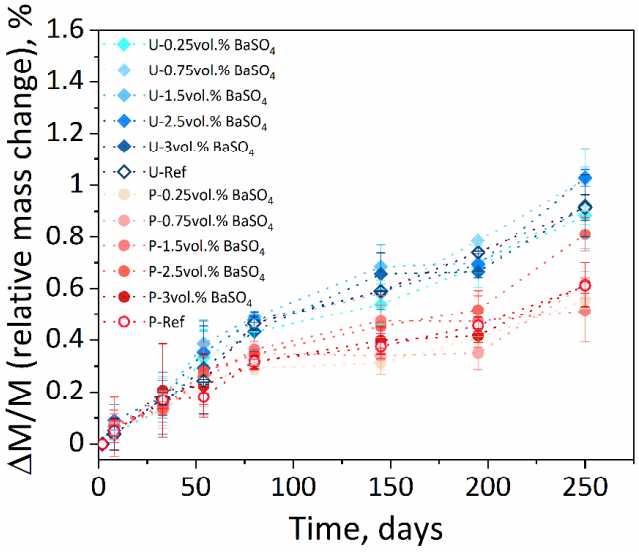

Figure S9. Evolution of the relative mass change for the specimens cast with the two aggregate types (blue shades for U, red shades for P) and with (filled markers) or without (hollow marker) $BaSO_4$. The markers indicate mean values while the error bars' size is the standard deviation of an ensemble of six distinct specimens, for each specimen set. The specimens for which these data were measured were

the same as those whose $\frac{\Delta L_Z}{L_Z}$ *values contributed to the data shown in Figure 3 within the article and in Figure S8 above.*

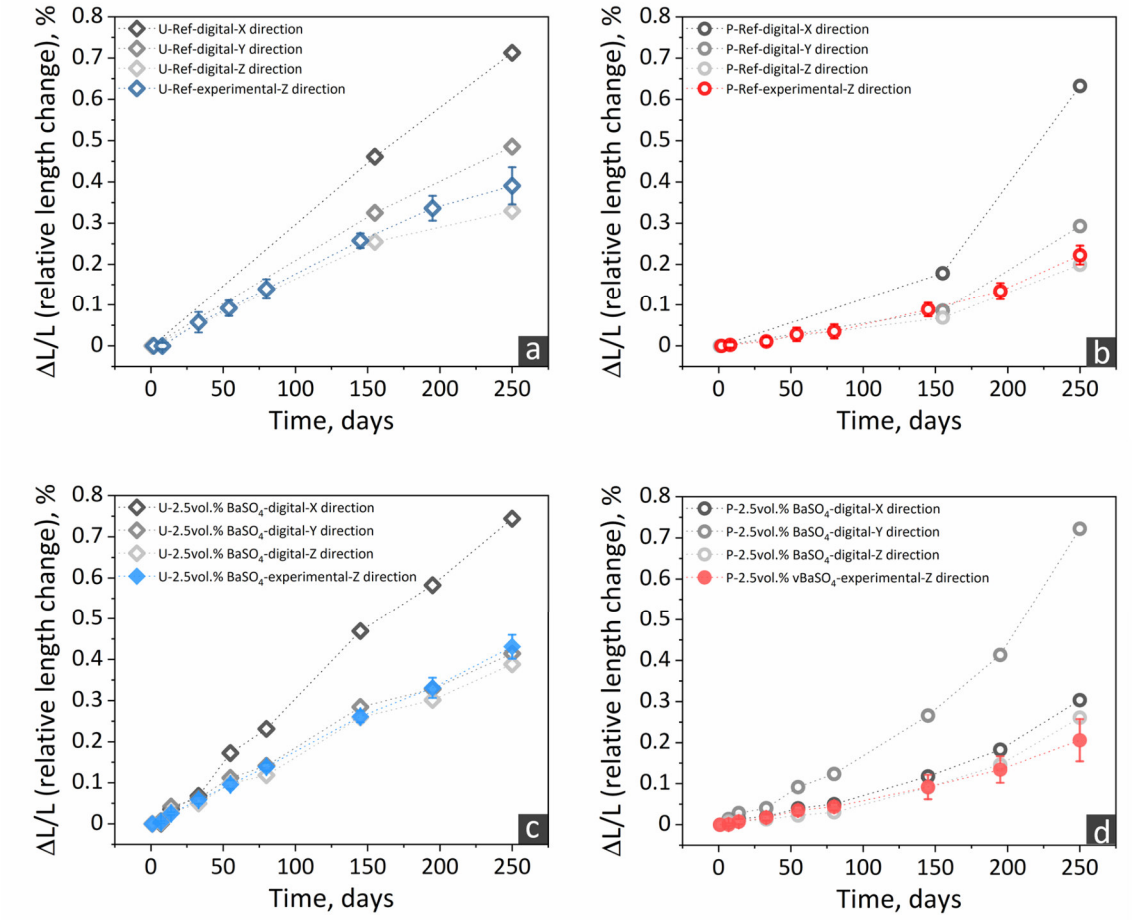

Figure S10. (a) Evolution of the relative size change for the tomographed volume of one of the six U reference specimens, computed along each axis from the the global affine registration results $(\frac{\Delta L_{AFF,k}}{L_{AFF,k}}, k = X, Y, Z$*, markers in grey tones, "U-ref-digital" label in the legend). The respective relative length change* $(\frac{\Delta L_{AFF,z}}{L_{AFF,z}})$ *is compared with the corresponding values measured for the whole specimen by the displacement gauge* $(\frac{\Delta L_Z}{L_Z}$*, blue markers, "U-ref-experimental" label in the legend). (b): similar plot as in (a) but for the tomographed volume of one of the six P reference specimens. (c) and (d): similar plots as in (a) and (b) but for the tomographed volume of one of the six specimens cast with 2.5 vol.-% BaSO₄. The color markers indicate the average of the six values while the associated error bar was computed as the respective standard deviation.*

The quasi-static, compressive Young's modulus evolution for some of the $BaSO_4$-containing specimens and for their corresponding reference specimens is presented in Figure S11. It was characterized, for all specimens, by the achievement of a peak value at about 15-20 days. Such an increase within the first 20 days could be attributed to the cement paste hardening

because of cement hydration. Even if ASR cracking might have already happened during this period, the microstructure formation due to cement hydration compensated its degradation effects. After about 20 days, the Young's modulus started to strongly and monotonically decline. After 150 days, the decrease rate slowed down, except for the P-ref specimens. The temporal evolution pattern characterized all the specimen types. The specimens cast with $BaSO_4$ followed an analogous evolution as their respective reference ones. At any time point and for any aggregate type, the differences between reference and $BaSO_4$-doped specimens were at a scale comparable with the data scatter range due to material heterogeneity. The P specimens exhibited smaller differences than the U ones, when comparing the results without and with $BaSO_4$.

As mentioned in Section 2.1.2 within the article, the replacement by $BaSO_4$ of an equivalent volume of aggregates led to a slight increase in specimen mass, for example a 1.44% and 1.46% mass increase at 3 vol.-% replacement, for the U and P aggregates respectively. In addition, since $BaSO_4$ resulted being well dispersed throughout the cement paste, as shown both in Figure 1 within the article and in Figures S1, S5 and S6, there exists the possibility of a stiffening effect of the cement paste. The Young's modulus time series in Figure S11 provide no systematic evidence of such a stiffening by the $BaSO_4$ addition: at any time point and for a given aggregate type, no systematic increase in Young's modulus was observed in correspondence of the increase in $BaSO_4$ concentration. The range of Young's modulus values, in the absence or in the presence of $BaSO_4$, was also similar to the range obtained in P-Ref and U-Ref specimens.

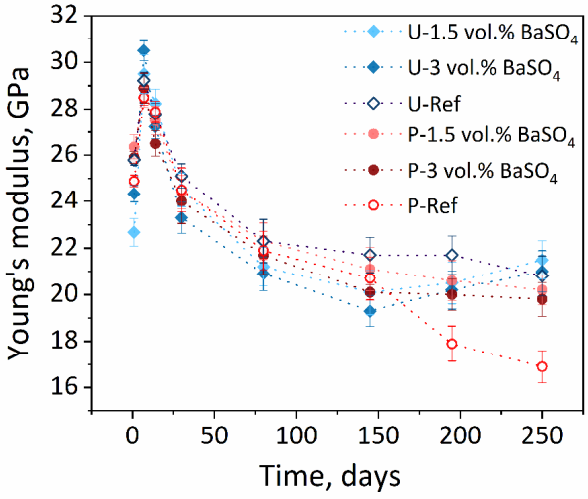

Figure S11. The time series of the quasi-static, compressive Young's modulus of specimens cast with both aggregate types, without or with two distinct $BaSO_4$ concentrations. The markers indicate mean values while the error bars size the standard deviation of an *ensemble* of three specimens (always the same at each time point), for each specimen set.

S1.6. ASR crack networks and correlated local deformations as assessed by time-lapse XT analysis

Reference specimens

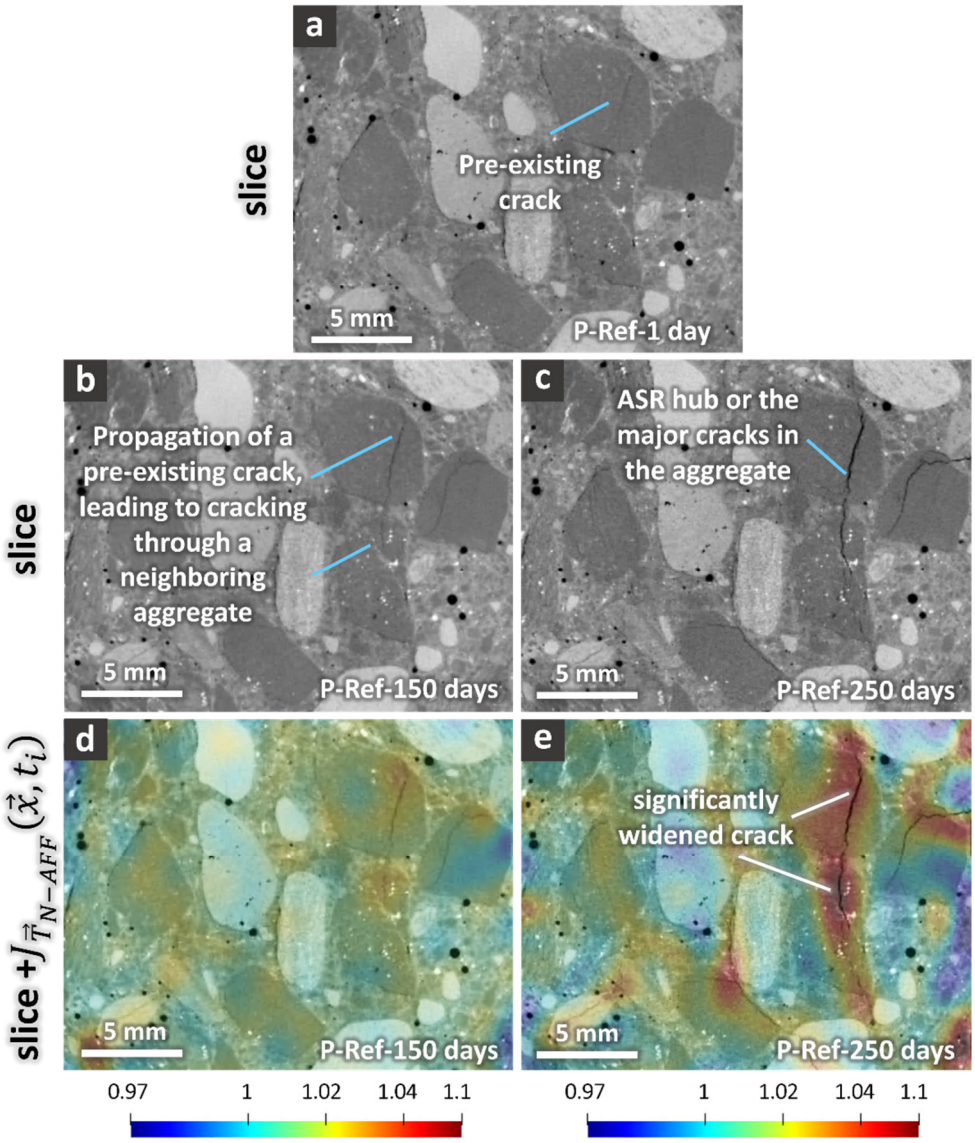

Figure S12. Visualization of the evolution of ASR cracks and associated localized deformations for the P-Ref specimen, by considering one slice from its tomographed volume, at multiple time points. The localized deformations are estimated by the determinant of the Jacobian matrix ($J_{\vec{T}_{N-AFF}}(\vec{x}, t_i)$) of the transformation vector field $\vec{T}_{N-AFF}(\vec{x}, t_i)$ associated with the non-affine registration. Its values larger than 1 indicate local volumetric expansion. Its values smaller than 1 indicate volumetric contraction. (a) X-ray tomogram at 1 day since start of the ASR acceleration. (b) and (c): slice at the

same position as in (a) but from the tomograms at 150 and 250 days, respectively. (d) and (e): the same slice as in (b) and (c), respectively, and, overlapped on top of it in a semi-transparent way, the slice at the same position but from $J_{\vec{T}_{N-AFF}}(\vec{x}, t_i)$ at the corresponding time points, respectively. The scale bars in (d) and (e) have, by definition of $J_{\vec{T}_{N-AFF}}$(relative volume), no unit.

Cracks in the reference specimens were segmented following the same TS-based procedure. Figure S13 and Figure S14 showcase the segmented, full crack networks, as solid objects rendered in 3D, at three distinct time points, for the U-Ref and P-Ref specimens, respectively. The parallelepiped box encompassing the crack networks indicates the tomographed volume of the specimens. The rendering views are exactly the same in all the rendered binary tomograms. The cracks seemed to be rather homogeneously distributed inside the tomographed volume. As time evolved, a larger crack volume fraction was achieved by both specimens.

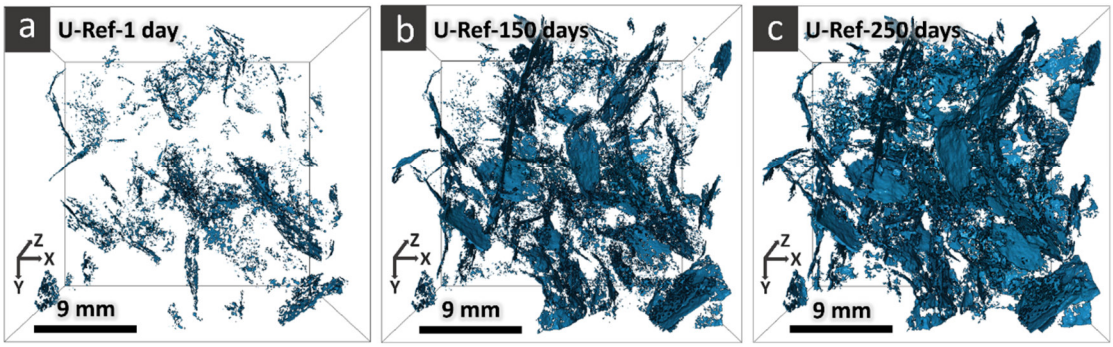

Figure S13. Temporal evolution of the crack network in the U-Ref specimen. (a)-(c): 3D rendering of the crack binary tomogram for the full tomographed volume of the specimen, at 1, 150 and 250 days, respectively

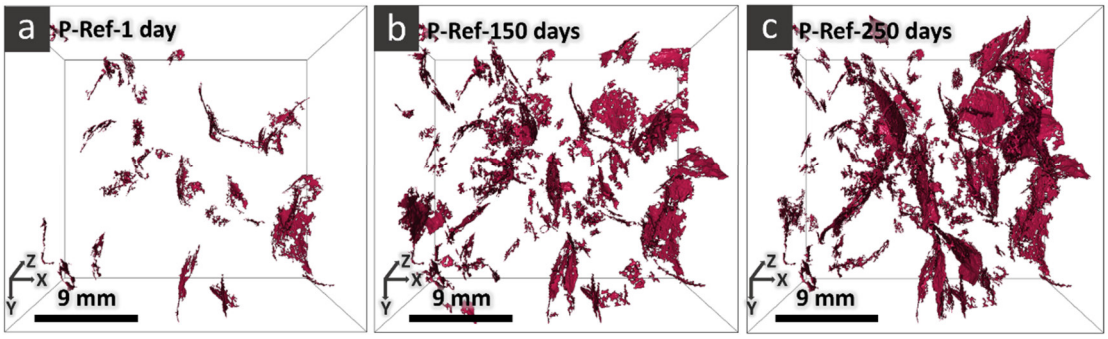

Figure S14. The same images as shown in Figure S13 but for the P-Ref specimen.

Specimens with $BaSO_4$

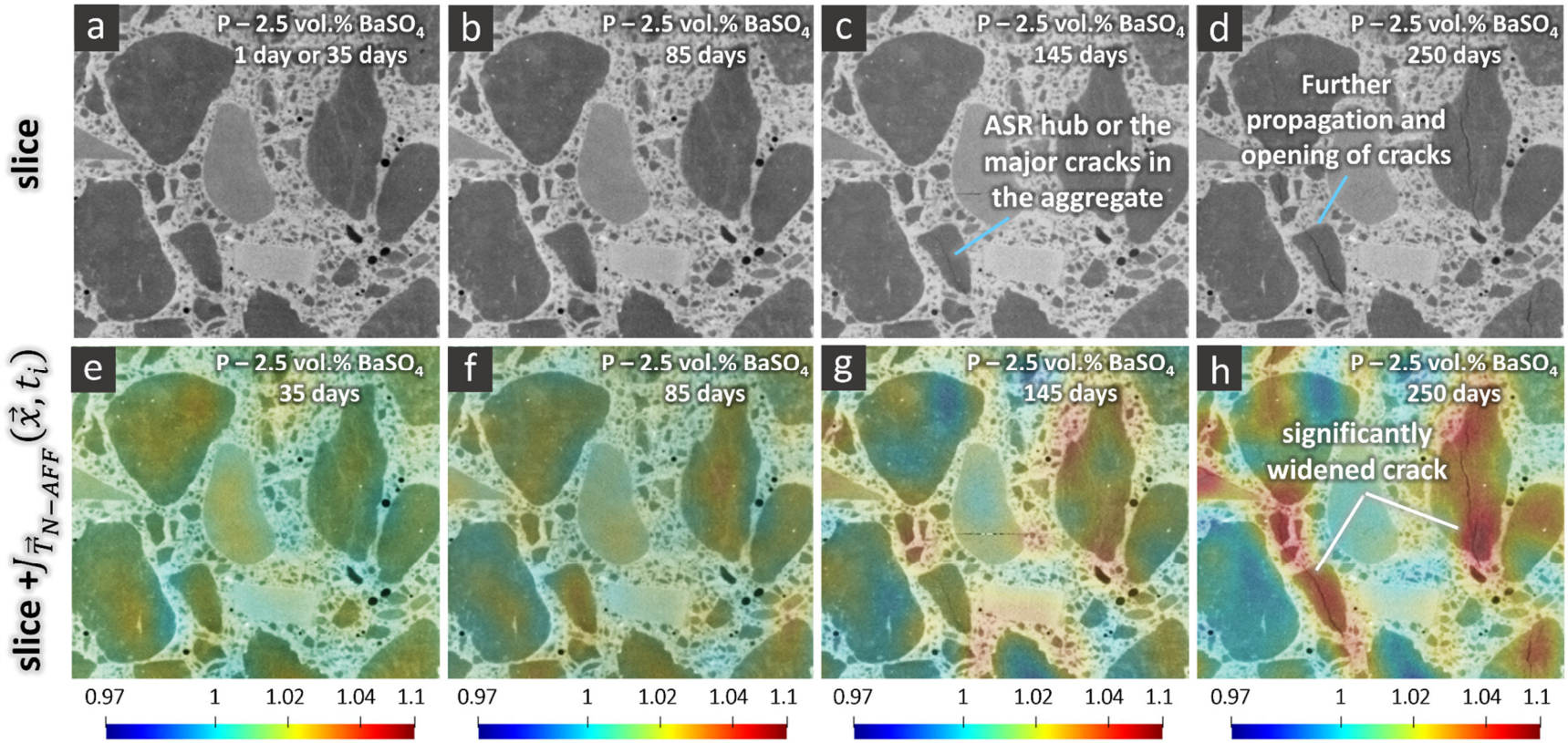

Figure S15. Similar visualization as in Figure 5 within the article but here for the P-2.5 vol.-% BaSO4 specimen. The chosen time points for the visualization are 35 days (insets (a) and (e)), 85 days ((b) and (f)), 145 days ((c) and (g)), 250 days ((d) and (h)). The tomograms did not change significantly between 1 day and 35 days. Thus, the one at 35 days was representative of the reference tomogram at 1 day.

The cracks in the specimens cast with $BaSO_4$ were segmented also by following the TS-based procedure. In addition to their segmentation, the availability of an additional label for each voxel, i.e., whether it belonged to aggregates or not, allowed classifying crack voxels also based upon whether they were inside aggregates or outside them.

Figures S16 and S17 show the time series of VOIs from the cracks binary tomograms, distinguishing by color their parts belonging to aggregate regions from their parts within the cement paste, for the U-2.5vol% $BaSO_4$. Figures S18 and S19 show analog 3D rendering for the P-2.5vol.% Ba SO_4 specimen.

3D rendering as those in Figures S16 to S19 allowed not only tracking the lengthening and widening of the cracks. It also allowed observing the coalescence of initially independent cracks and the percolation of the resultant network. The latter is an intrinsic 3D process, thus not observable by the mere slice inspection. In addition, because of the aggregate segmentation, it is possible to observe by such rendering that the crack propagation through the paste played a significant role in the crack network percolation. This feature can be appreciated, for example, by observing the crack evolution throughout the paste from 85 days to 250 days in Figure S17 (c) and (d), respectively.

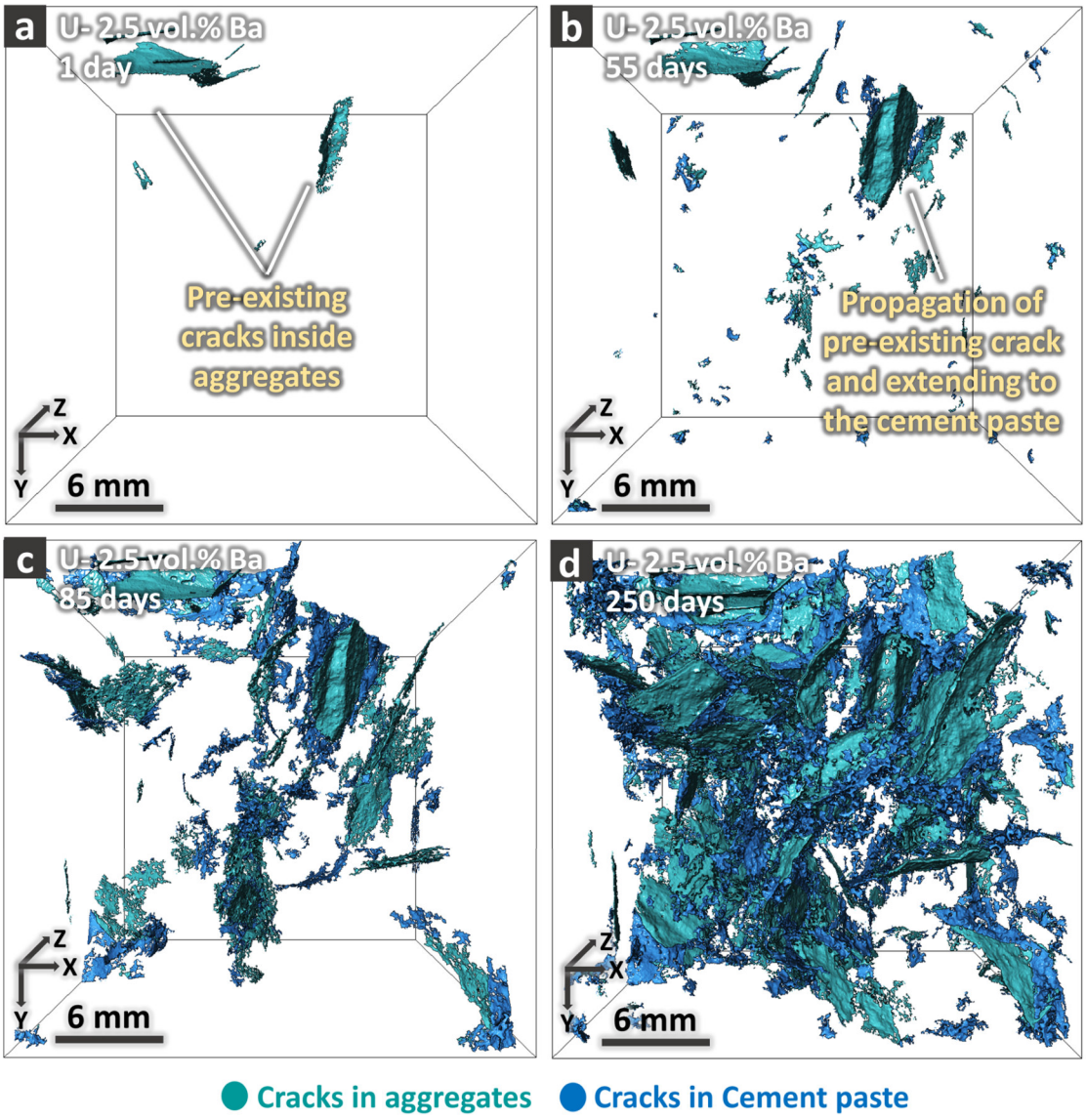

Figure S16. A small VOI of the binary tomograms of cracks inside aggregates (cyan) and in the cement paste (blue) is rendered at distinct time points for the U-2.5 vol.-% $BaSO_4$ specimen. Such VOI contained cracks, which were nucleated in an aggregate and further propagated into the surrounding cement paste. The insets from (a) to (d) correspond to different time points during the ASR acceleration, including 1 day, 55, 85 and 250 days, respectively. The viewpoint of the 3D rendering in each inset was kept the same.

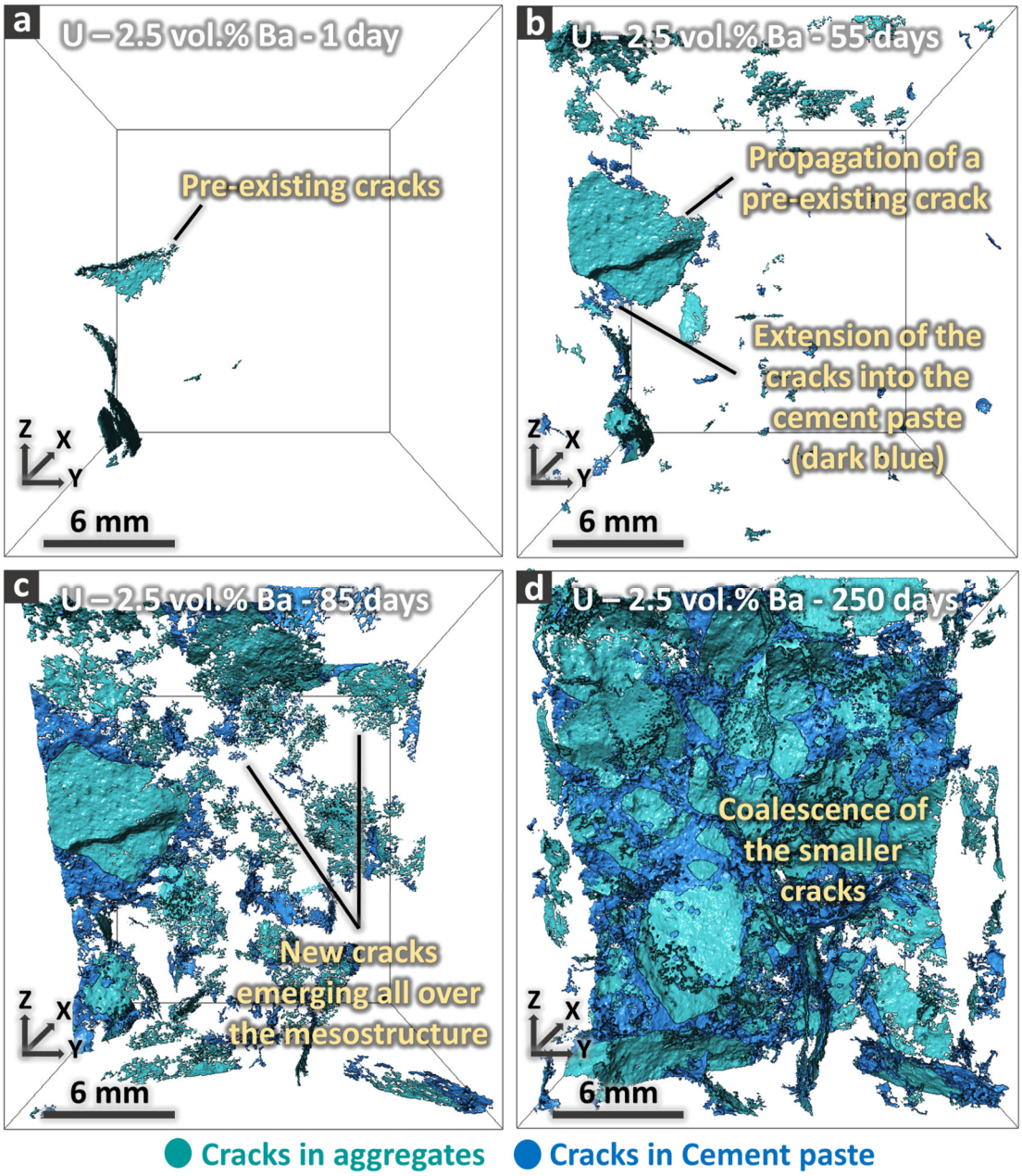

Figure S17. Similar visualiaztion as in Figure S16 but for a distinct VOI.

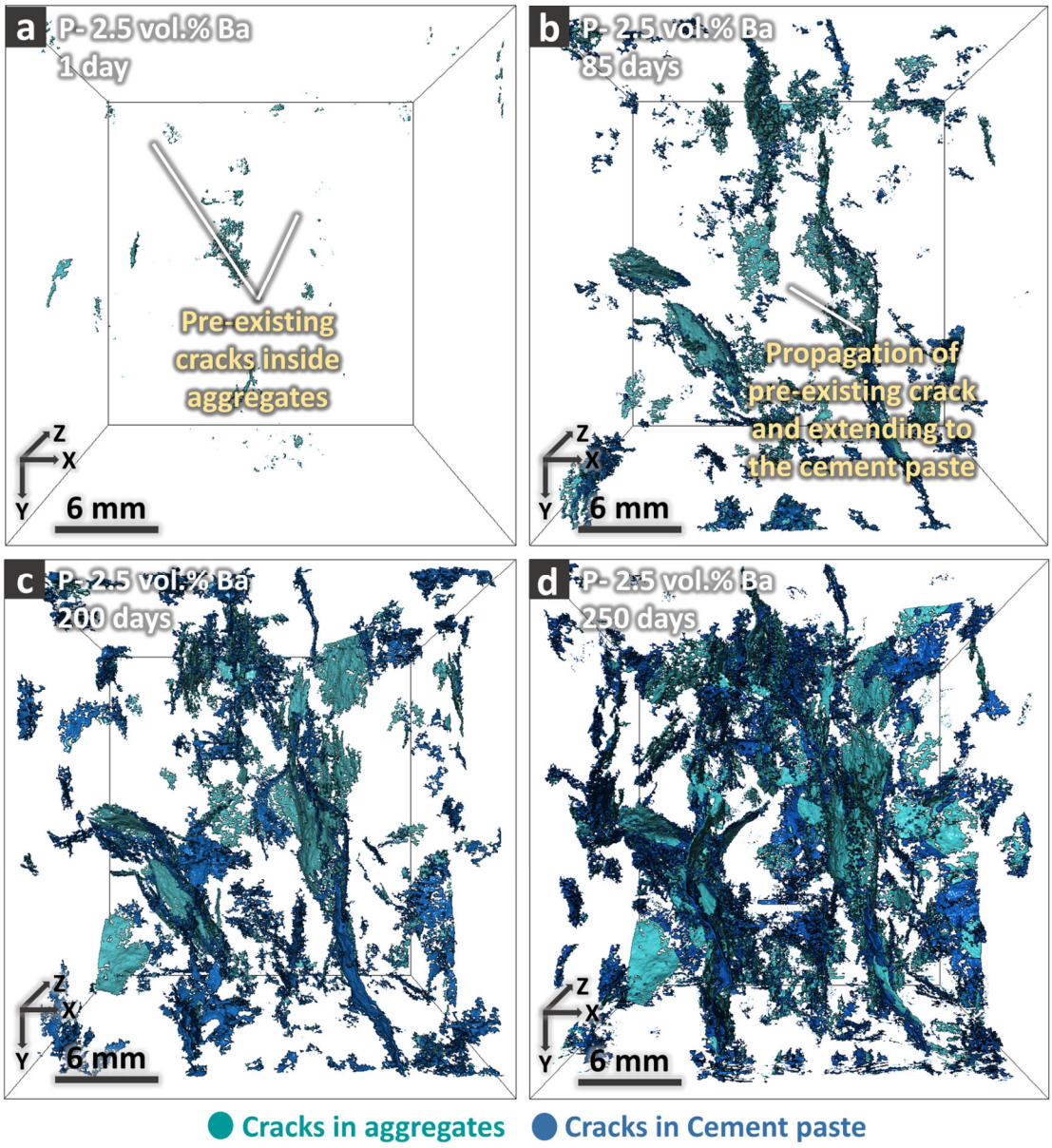

Figure S18. Similar visualization as shown in Figure S16 but for the P-2.5 vol.-% $BaSO_4$ specimen and at ((a) to (d)) 1, 85, 200 and 250 days, respectively.

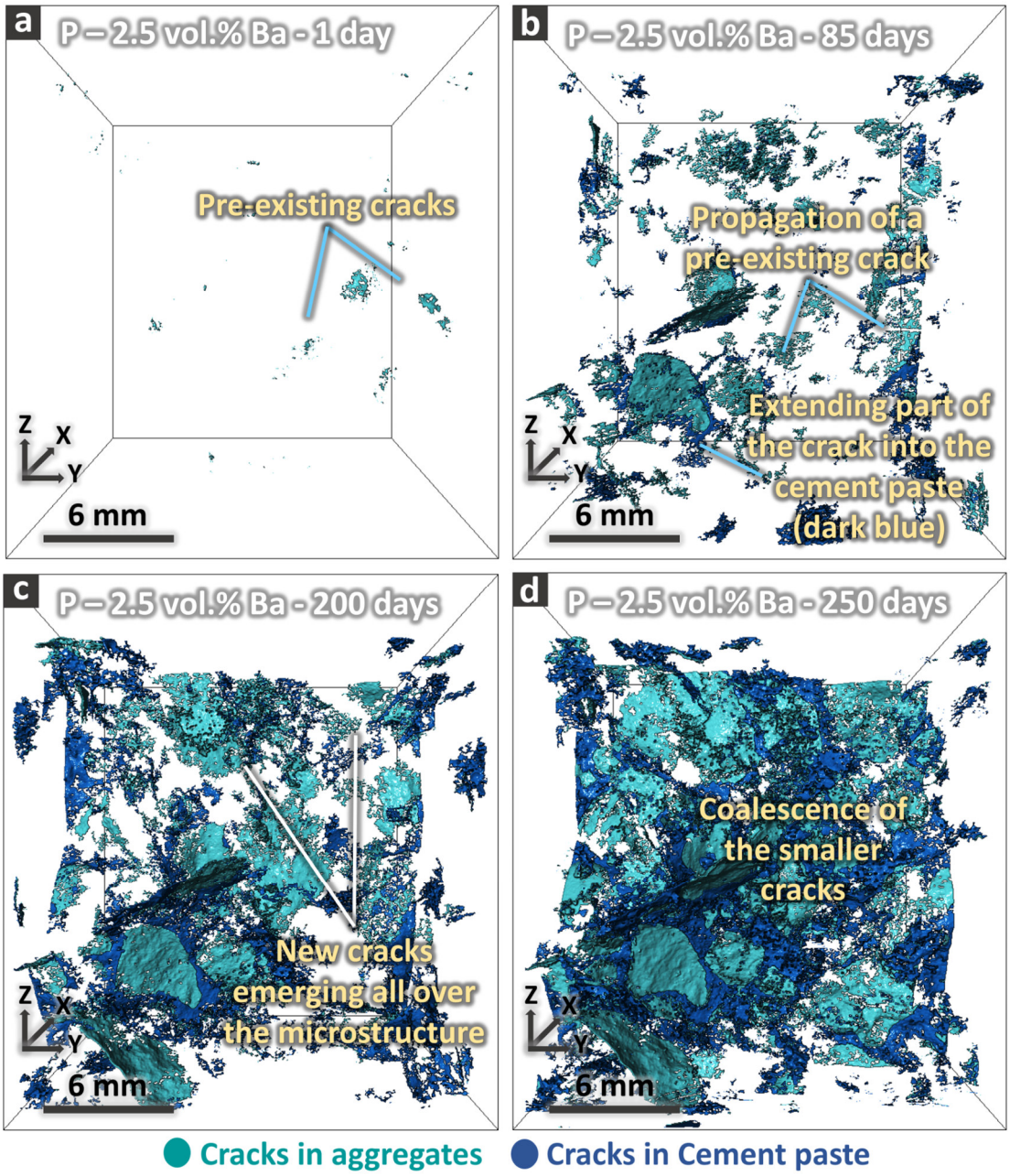

Figure S19. Similar visualization as in Figure S18 but for a distinct VOI.

S1.7. Quantitative volumetric analysis of the ASR crack networks

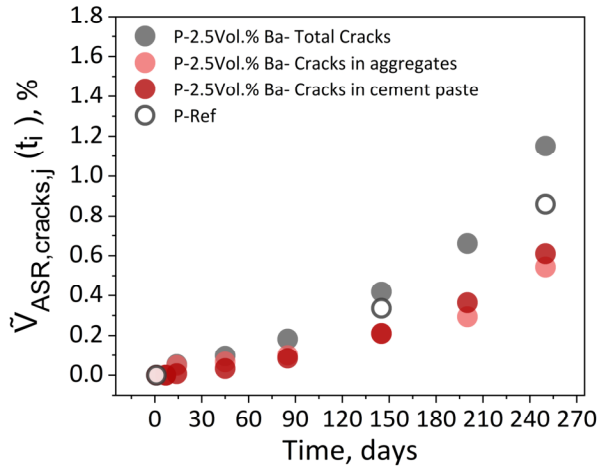

Figure S20. Quantitative comparison of the ASR cracking in different specimens based on the estimates of two variables: (1) the total volume of ASR-induced cracks (filled grey markers for the P-2.5 Vol.% $BaSO_4$ specimen and empty grey markers for the reference one) and those only in aggregates (lighter blue, filled markers) or cement paste (darker blue, filled markers), normalized by the tomogram volume, named as $\tilde{V}_{ASR,cracks,j}$.

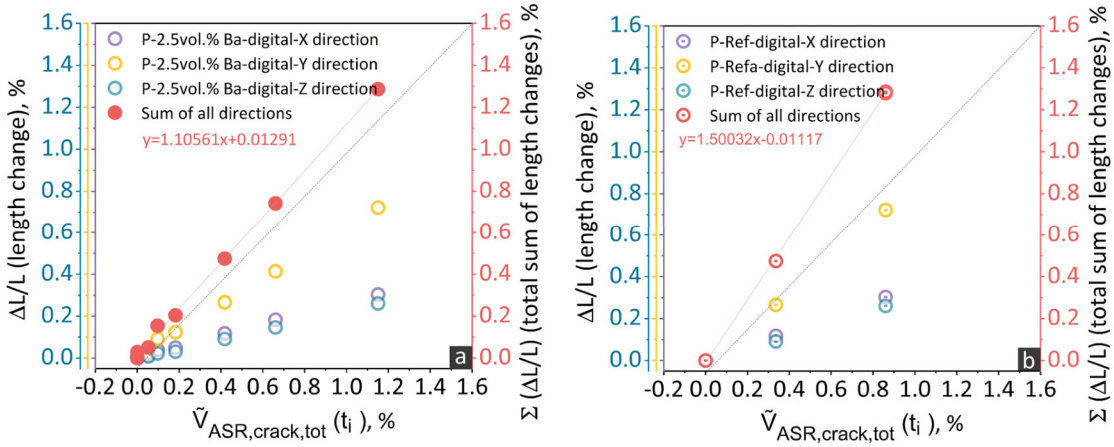

Figure S21. (a) Correlation between the ASR cracks total volume fraction, $\tilde{V}_{ASR,cracks,tot}$, and the relative volume change computed for the tomographed regions of the P specimen containing $BaSO_4$. The relative volume change was estimated approximately as $\sum_{k=X,Y,Z}\frac{\Delta L_{AFF,k}}{L_{AFF,k}}$, where $\frac{\Delta L_{AFF,k}}{L_{AFF,k}}$, with $k = X,Y,Z$, is the relative size change of the region as estimated from the results of the global affine registration. The dotted line indicates the $y = x$ line of the $\left(\tilde{V}_{ASR,cracks,tot}; \sum_{k=X,Y,Z}\frac{\Delta L_{AFF,k}}{L_{AFF,k}}\right)$ plane. (b) Similar graph to what shown in inset (a), but for P-Ref specimen.

S1.8. Shape tensor analysis of the separated cracks

Figure S22 (a) shows the 3D rendering of the segmented, total crack network of the U-Ref specimen at 250 days. Distinct, disconnected cracks are rendered with different colors. Despite a great complexity, several cracks could be clearly distinguished, which indicates that the crack network labelling managed to recognize the distinct cracks.

The shape tensor analysis was carried out at distinct time points on the segmented cracks of each tomographed specimen, to quantitatively characterize their shape and orientation. Figure S22 (b) shows the 3D rendering of a single crack extracted from the labelled binary tomogram of the total crack network rendered in inset (a), to serve as an example for the shape of an isolated ASR crack and its shape tensor. The three *eigen*vectors of the crack are also rendered as solid arrows, starting from the center of mass of the crack itself.

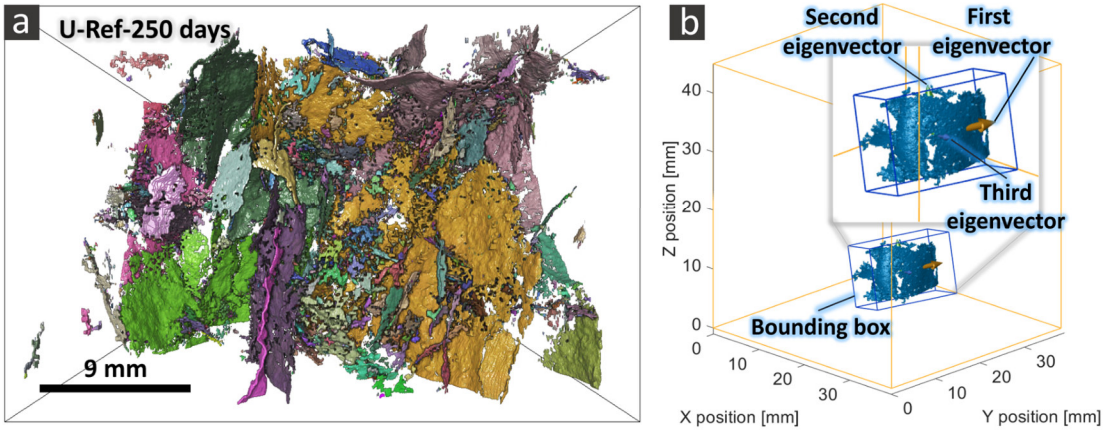

Figure S22. (a): 3D rendering of the segmented, total crack network of the U-Ref specimen, at 250 days. Each separated part (branch) of the crack network is rendered with a distinct color, just for the purpose of distinguishing it from the other ones. The color assignment to each branch was random. (b) A single separated crack from the networks shown in (a). The large parallelepiped box highlighted in orange delineates the tomographed region. The smaller grey box shows a zoom-in view of the respective crack. The blue, parallelepiped box is the crack's bounding box oriented according to the three eigenvectors of the crack's shape tensor $\boldsymbol{G}$*. Each eigenvector, located at the center of mass of the crack and scaled by half the lateral size of the bounding box along the same direction, is also rendered as a solid arrow. The red arrow refers to the eigenvector associated with the* 1^{st} *eigenvalue. The green arrow refers to the second eigenvector and the blue one to the third.*

S2. Extensive quantitative analysis of specimens with $BaSO_4$ and $CsNO_3$ concentrations

S2.1. Macroscopic dimensional changes and mass evolution

The $BaSO_4$ addition (at different concentrations) in specimens cast also with $CsNO_3$ had a very small effect on the expansion along the Z-axis, consisting in slightly higher average $\frac{\Delta L_z}{L_z}$ values, starting from about 140 days, compared with the specimens cast with no $BaSO_4$, as observable in Figure S26 (a). However, the difference in the average value at each time point was smaller or of the same magnitude as the error bars'. When comparing the specimens cast with distinct $BaSO_4$ concentrations, no systematic variation of the $\frac{\Delta L_z}{L_z}$ time series with the increasing $BaSO_4$ concentration could be observed, as it was already the case for the specimens cast without $CsNO_3$ (see Figure 3 in the article). At any time point, $\frac{\Delta L_z}{L_z}$ fluctuated randomly with increasing $BaSO_4$ concentration. The fluctuation amplitudes were significantly smaller than the range defined by the computed error bars. The maximum average expansion of the $BaSO_4$-free specimens, labelled as U-Cs 0 vol.-% Ba in Figure S26, was about 13% larger than the one achieved by the U-Ref specimens (see Figure 3 in th article). Such expansion boosting effect by the $CsNO_3$ presence was already observed in our previous study [3], [4]. There, it was already shown that the main Cs-doping influence was an increase in the ASR kinetics, which manifested itself as a faster expansion.

Along the two lateral (i.e., X- and Y-) axes, the expansion was larger than or similar to the one along the Z-axis, as showcased for one specimen, U-Cs-1.5 vol.% $BaSO_4$, in Figure S26 (b), estimated based upon the results of the affine registration. This result mirrors what already systematically observed in previous specimens, including for specimens cast only with $BaSO_4$ (see the example in Figure S10 (c) for a specimen cast with 2.5 vol.-% $BaSO_4$ and no $CsNO_3$).

The relative mass changes of the same six specimens of Figure S26 (a) also did not considerably vary with different $BaSO_4$ concentrations and in the presence of $CsNO_3$. See Figure S27. Therefore, the concurrent presence of $CsNO_3$ and $BaSO_4$ seems not to have perturbed, within the used range of $BaSO_4$ concentrations, the previously observed ASR expansion for specimens cast with $CsNO_3$ and the effects of the latter on expansion itself.

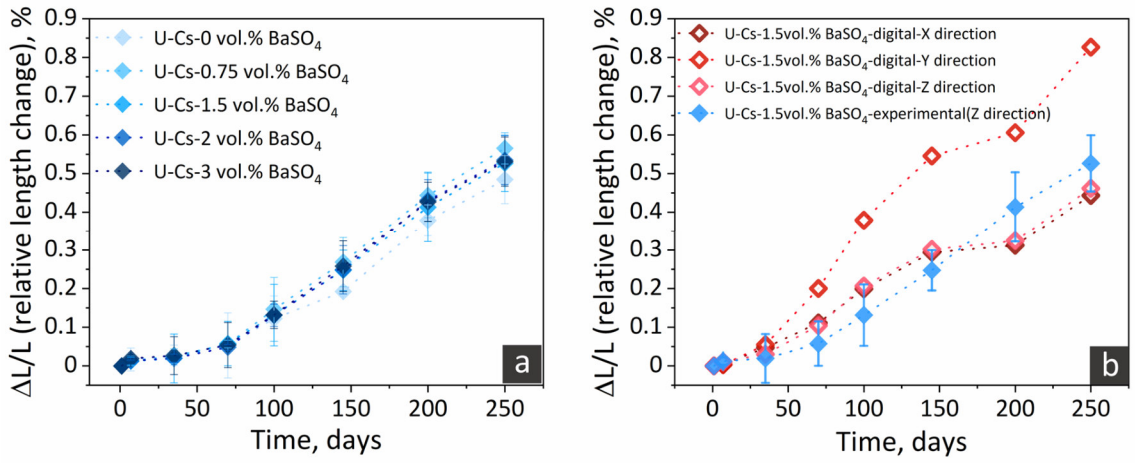

Figure S26. (a): evolution of the relative length change, along the specimen longitudinal direction (Z-axis) and measured experimentally ($\frac{\Delta L_z}{L_z}$), of distinct specimens cast with U aggregates, the fixed $CsNO_3$ concentration and distinct $BaSO_4$ concentrations. The markers indicate averages while the error bars size is the standard deviation of six values from an ensemble of six distinct specimens, for each specimen set, i.e., $BaSO_4$ concentration. (b): comparison between the experimentally measured $\frac{\Delta L_z}{L_z}$ of the six specimens and the relative length change, along any axis of the Cartesian frame of reference and of another specimen, cast with the optimal $BaSO_4$ of 1.5 vol.-%, computed from the results of the affine registration (labelled as digital), $\frac{\Delta L_{AFF,k}}{L_{AFF,k}}, \forall\, k = X, Y, Z$.

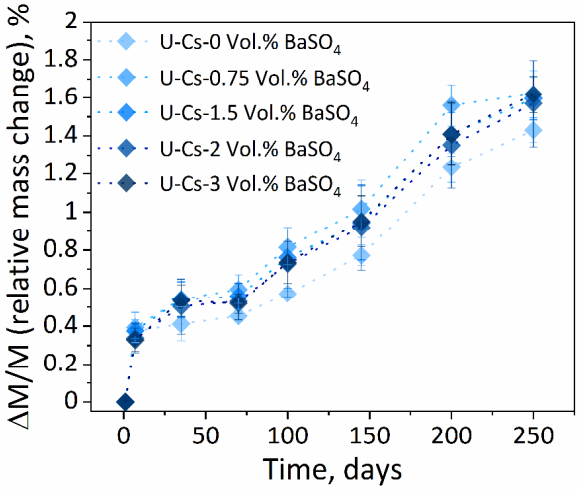

Figure S27. Evolution of the relative mass change of distinct specimens cast with U aggregates, $CsNO_3$ (at fixed concentration) and various $BaSO_4$ concentrations. The markers indicate averages while the error bars' size is the standard deviation of six values from an ensemble of six distinct specimens, for each specimen set.

S2.2. Time-lapse XMT

Figure S28 and Figure S29 provide two examples of selected ROI slices from the tomogram of the U-Cs-1.5vol.% Ba specimen, at four distinct time points specified on each slice.

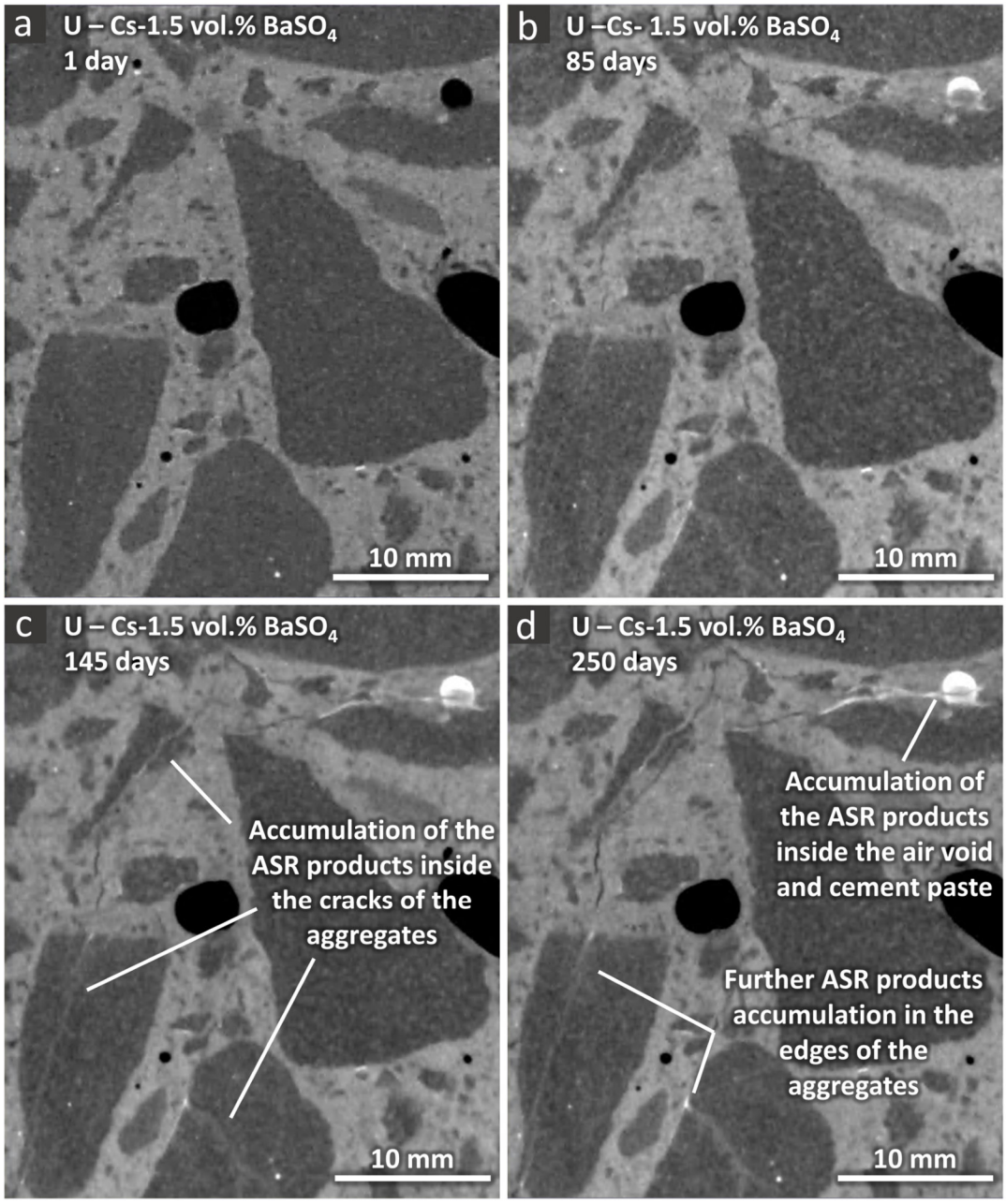

Figure S28. Temporal evolution of the crack network in the U-Cs-1.5 vol.-% $BaSO_4$ specimen. (a)-(d): on one $(X-Y)$ slice of the tomograms at 1, 85, 145 and 250 days, respectively. The position of the slice and of the ROI on it is the same at any time point.

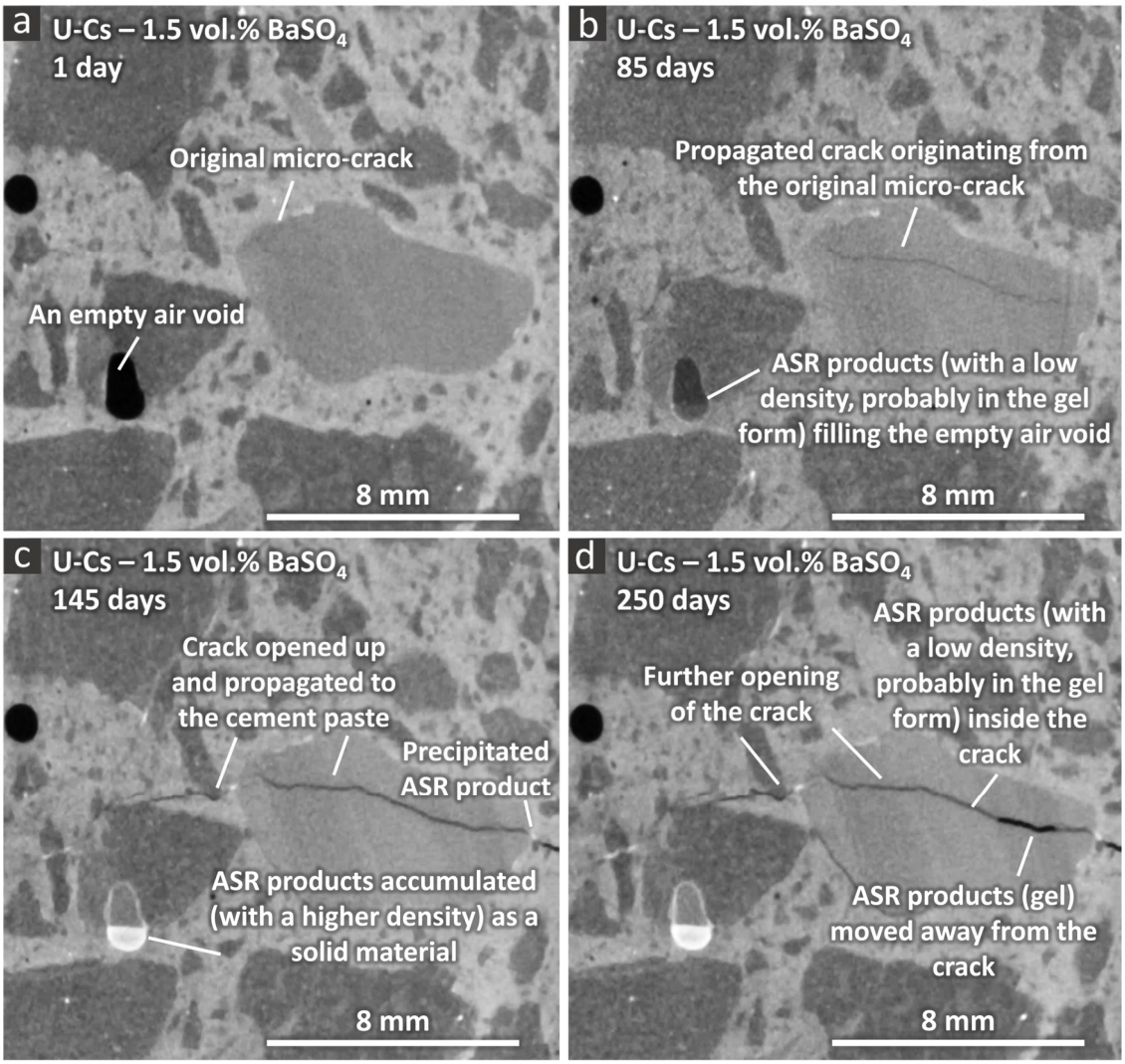

Figure S29. Similar figure as S28 but considering another ROI on a distinct slice of the tomograms of the U-Cs-1.5 vol.-% $BaSO_4$. The dynamic range of the visualization of the slices was different from the one in Figure S28, to better highlight certain features.

Figure S30 showcases some qualitative features of the correlations between the cracks' and the products' spatial distributions, using the combined and separated rendering of the segmented cracks (with or without products) and other pores filled with products. The visualization in this case refers only to the state of the U-Cs-1.5 vol.-% $BaSO_4$ specimen at 250 days. While in inset (a), all four binary tomograms are shown together, each rendered with a distinct color, insets (b) and (c) show separately the binary tomograms of products and of empty cracks, respectively. These distinctly rendered binary tomograms allowed noticing several qualitative features. From Figure S30 (b), it could be already inferred that ASR products likely existed in almost equal amounts within the aggregates and within the cement paste. In addition, it can

be seen that much of the ASR products within the cement paste were accumulated inside large air voids (Figure S30 (b)).

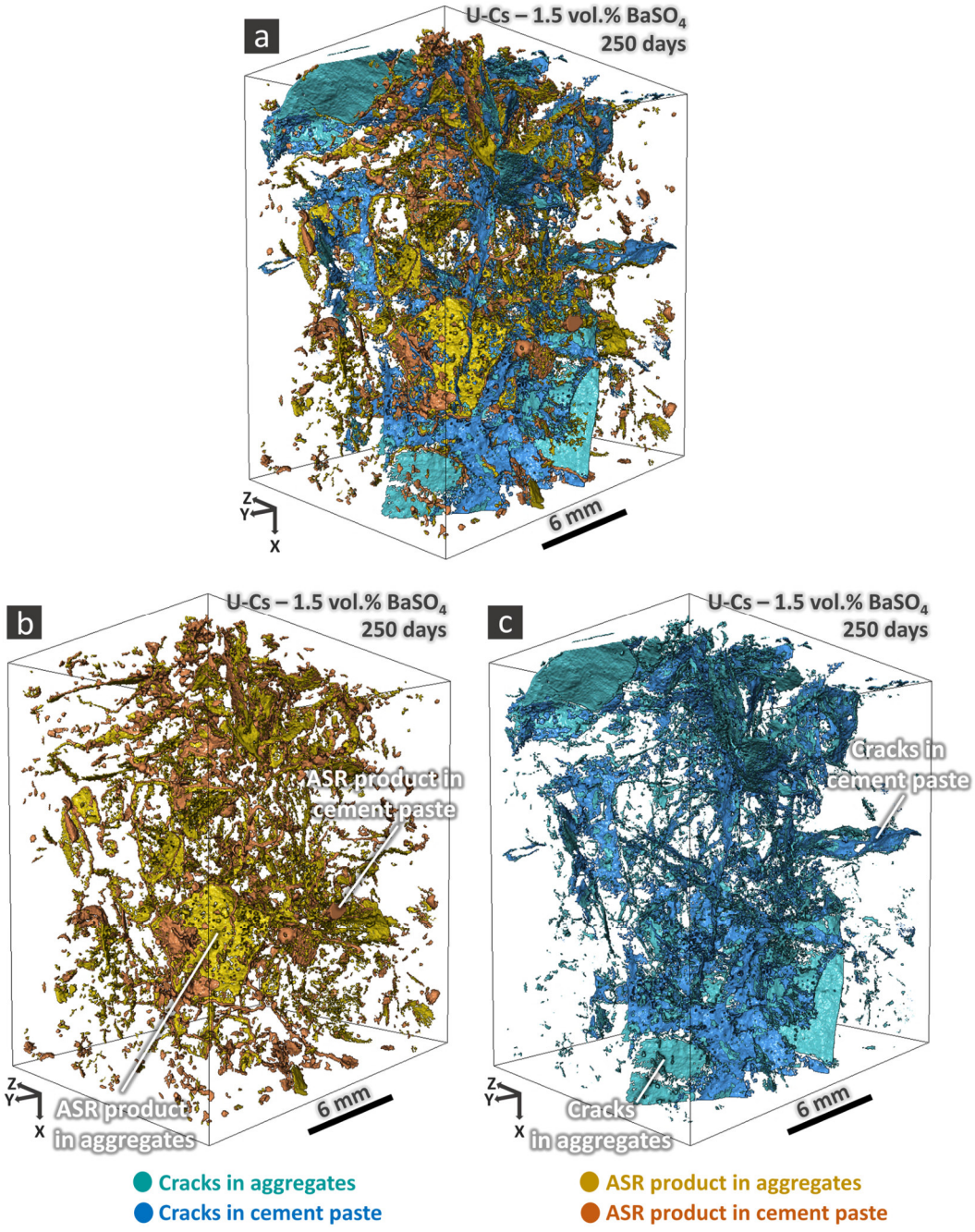

Figure S30. 3D rendered volumes of interest (VOIs) from the binary tomograms of empty cracks either inside aggregates (cyan) or within the cement paste (blue) and of ASR products in the entire part of the pore space resolved in the tomograms (e.g., spherical air voids, porous patches and cracks), with distinction between regions inside (yellow) and outside (orange) of aggregates. The analyzed tomogram was the one of the U-Cs-1.5 vol.-% $BaSO_4$ at 250 days. (a): rendering of the VOI of all four types of

binary tomograms (ASR products inside and outside aggregates and empty cracks inside and outside aggregates) together. (b): rendering of the VOI of only the two ASR products binary tomograms. (c): rendering of the VOI of only the two binary tomograms of empty cracks.

S2.3. Shape tensor analysis of the crack network in the absence and presence of both contrast agents ($CsNO_3$ and $BaSO_4$)

The elongation, E, *versus* flatness, F, plots at the first and last (250 days) time points of both the U-Ref and of the U-Cs-1.5 vol.-% $BaSO_4$ specimens (Figure S31) showed that the presence of both $CsNO_3$ and of $BaSO_4$ did not have any kind of significant influence on the crack shape, which remained prevalently that of a thin, curved plate, as observed for all the specimens of any experimental campaign.

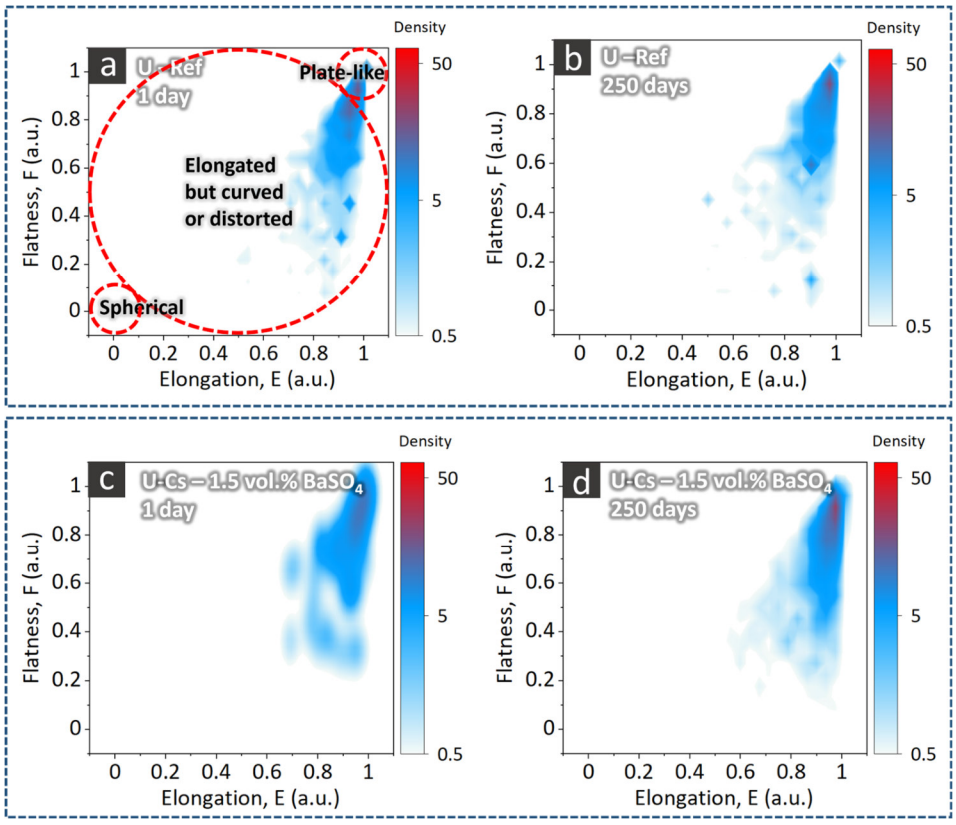

Figure S31. Plots of the kernel density estimate (KDE) of the joint probability density function (PDF) of the two shape feature variables, the elongation E and the flatness F, computed from the shape tensor analysis of the segmented total crack network and treated as a bi-variate random variable, $(\mathbb{E};\mathbb{F})$. (a) and (b): U-Ref specimen. (c) and (d): U-Cs-1.5 -vol.% $BaSO_4$ specimen.

The 3D distribution of the first *eigen*vector, $\hat{u}_1$, of the shape tensor $\boldsymbol{G}$ for the same two specimens as for the shape analysis of Figure S31 and at the first and last time points as well (Figure S32) confirmed that the simultaneous presence of $CsNO_3$ and $BaSO_4$ in the mix designed seemed not to have altered the typical crack orientation features systematically observed across the distinct experimental campaigns and for distinct specimen types. For both specimens, at the first time point (i.e., in the presence of only original cracks), a rather uniform and relatively sparse crack orientation distribution could be observed. However, at the last time point, the crack networks of both specimens exhibited a slight tendency for being aligned along the Z-axis. Even a slight preferential crack orientation along the specimen longitudinal direction (the Z-axis), automatically implies that the crack thickness increase with time contributed more to the specimen dimensional changes in directions orthogonal to that axis than along it, which is exactly what was observed for both specimens (see Figure S8 (c) for the U-Ref specimen and Figure 26 (b) for the U-Cs-1.5 vol.-% $BaSO_4$ one).

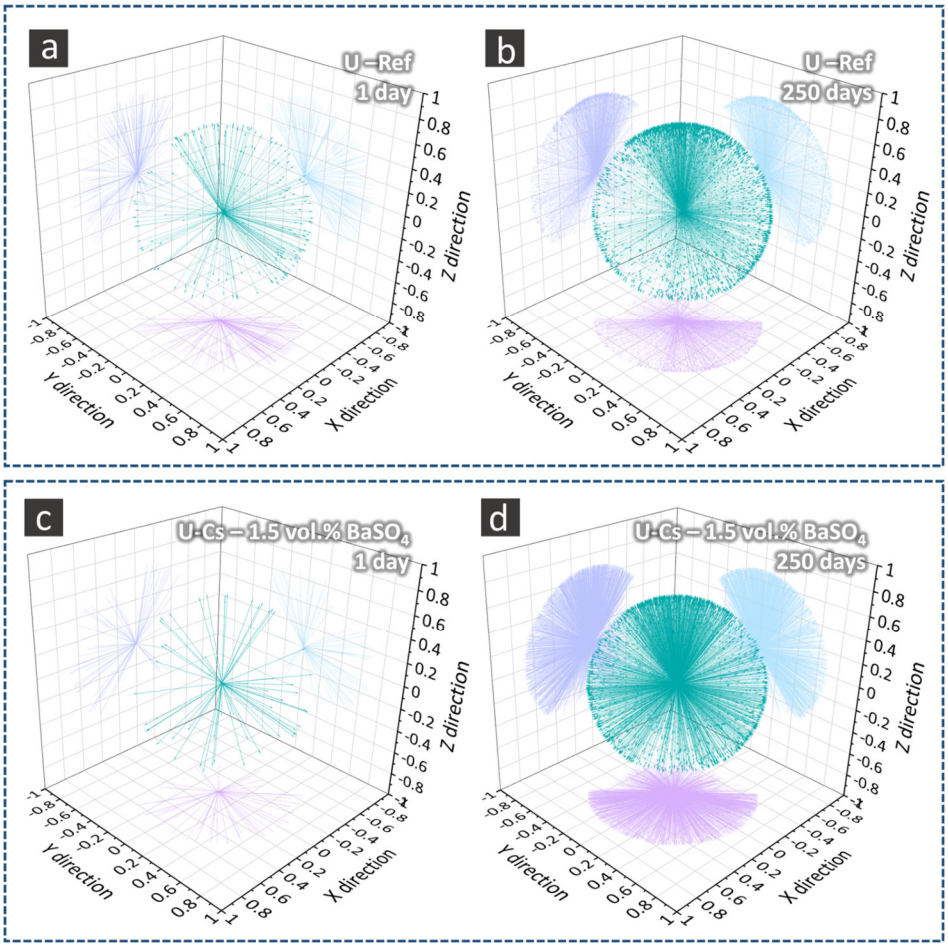

Figure S32. Visualization of the crack orientation analysis results. The crack orientation was operatively defined as the direction of the eigenvector $\hat{u}_1$ associated with the first and largest eigenvalue of the

shape tensor $\boldsymbol{G}$. The segmented total crack network of a specimen corresponded to a set of $\hat{u}_1$'s, one for each independent crack (branch of the network). Each of these vectors are here plotted in red, after rescaling their magnitudes by a factor equal to 0.33, to make their projections on the planes of the Cartesian frame of reference more visible. The projections of $\hat{u}_1$ on the $X-Y$ plane are in violet, those on the $X-Z$ plane are in dark blue and those on the $Y-Z$ plane are in light blue. (a) and (b): U-Ref specimen, at 1 and 250 days, respectively. (c) and (d): U-Cs-1.5 vol.-% $BaSO_4$ specimen, at 1 and 250 days as well, respectively.

Bibliography

[1] P. Carrara *et al.*, "Improved mesoscale segmentation of concrete from 3D X-ray images using contrast enhancers," *Cem. Concr. Compos.*, vol. 93, pp. 30–42, Oct. 2018, doi: 10.1016/j.cemconcomp.2018.06.014.

[2] R. Kresse *et al.*, "Barium and Barium Compounds," *Wiley-VCH Verlag GmbH Co. KGaA (Ed.), Ullmann's Encycl. Ind. Chem. Wiley-VCH Verlag GmbH Co. KGaA, Weinheim, Ger.*, pp. 621–640, 2007, doi: 10.1002/14356007.A03_325.PUB2.

[3] M. Shakoorioskooie, M. Griffa, A. Leemann, R. Zboray, and P. Lura, "Alkali-silica reaction products and cracks: X-ray micro-tomography-based analysis of their spatial-temporal evolution at a mesoscale," *Cem. Concr. Res.*, vol. 150, p. 106593, Dec. 2021, doi: 10.1016/J.CEMCONRES.2021.106593.

[4] M. Shakoorioskooie, M. Griffa, A. Leemann, R. Zboray, and P. Lura, "Supplementary data/materials for the article: 'Alkali-silica reaction products and cracks: X-ray micro-tomography-based analysis of their spatial-temporal evolution at a mesoscale,'" May 2021, doi: 10.5281/ZENODO.4837142.